

Flexible, Sensitive, Multifunctional Rubber-based Sensor with Multiple Responses to Infrared, Temperature, Humidity and Strain

Zhongjie Zheng

Guangxi University

Li Yang

Guangxi University

Yunpeng Yang

Guangxi University

Baofeng Lin

Guangxi University

Lihua Fu

Guangxi University

Chuanhui Xu (✉ xuhuiyee@gxu.edu.cn)

Guangxi University

Article

Keywords:

Posted Date: December 10th, 2021

DOI: <https://doi.org/10.21203/rs.3.rs-1158489/v1>

License:   This work is licensed under a Creative Commons Attribution 4.0 International License.

[Read Full License](#)

Abstract

Flexible wearable electronic sensors have attracted immense interest in human motion detection, body temperature monitoring and personal healthcare monitoring. However, most of reported sensors cannot integrate multifunctional applications at the same time though they own excellent single achievement of strain sensing or humidity sensing. Herein, we fabricate a multifunctional rubber-based flexible sensor (MRFS) with responses to infrared, temperature, humidity and strain. The sensor owns a superior strength (5.66 MPa), high stretchability (367%), high temperature coefficient of resistance (2.046%/°C) and high photothermal conversion efficiency (78.6%). For the sensing applications, it shows a rapid sensing of only 0.5 s for the temperature and humidity changes as well as a sensitive response to low-powered near infrared of 0.14 W/cm², body temperature change from 33.6 to 35.6 °C, and small amount of moisture on human skin. Moreover, the MRFS shows a considerable strain sensing for human joint motion and an antibacterial property.

1. Introduction

Skin, the largest organ on the human surface, plays a pivotal role in the daily interaction with the environment. It not only protects internal tissues from the invasion of harmful bacteria and virus, but also can feel the sun light, temperature, humidity and pressure, making us comprehend the world better.¹ In recent years, it has been great interesting in designing and fabricating multifunctional sensors to replace the skin sensing so that the sensors can be used for the organ of biomimetic robot. These sensor devices have a promising application in a wide range of physical condition sensing, personal motion detection, flexible electronic screen and living environment monitoring.² To meet the requirements of these applications, the sensor devices are required to be flexible and stretchable possibly. As a result, there has been considerable effort in developing various flexible materials to achieve sensor devices for monitoring temperature, humidity, strain, pressure, and so on in the past few years. Rubber, a flexible and elastic material with the advantages of low cost and easy processing, has been widely used in all aspects of our life since the last century.³ Nowadays, it seems to be an appropriate material served as the sensor's matrix to endow the sensor with flexibility. To achieve this goal, incorporation of conductive filler into rubber, such as carbon nanotubes (CNT)⁴, graphene⁵ and metal⁶, is an effective method to form a successive conductive pathway, converting external stimuli into accurate electrical signals. For example, Lin et al. prepared a carboxylated styrene-butadiene rubber (XSBR)/CNT flexible sensor which owned a low detection limit of 1% and high sensitivity with a gauge factor up to 25.98⁷. The rubber-based strain sensor had sensitive response to low strain (smile and breathing) as well as high strain (human motion). Liu et al. developed a ZnCl-decorated epoxidized natural rubber (ENR)/CNT strain sensor with a self-healing ability, which can detect multiple tiny signals, such as coughing, pronunciation, and deep breathing⁸. On balance, the strain sensing is most general application for rubber-based sensors due to its flexible and stretchable properties. Therefore, realization of multifunctional application in rubber-based sensors is a crucial challenge due to the rapid development of artificial intelligence technology.

Compounding with other functional materials is simple and effective method to obtain multifunctional applications for rubber-based sensor⁹. At the background that concept of sustainable development has been deeply rooted among the people, natural polymer is a potential candidate for multifunctional sensor designing. Especially, the natural polymer containing larger amount of hydroxyl groups is hydrophilic, which can catch water molecule by hydrogen bounding and thus improve water diffusion¹⁰. For example, Li et al. developed a humidity/infrared-sensitive intelligent actuator by self-assembled cellulose nanocrystals film and polyurethane (PU) substrate with synergistic structural color changes¹¹. Under the humidity environment, the color of intelligent actuator could achieve a way of color-changing from blue to brown at $t = 9$ s; conversely, the color returned to blue at $t = 104$ s. Yao et al. prepared chiral nematic nanocrystal/poly(ethylene glycol) composites which could change the color in different humidity¹². As relative humidity (RH) increased gradually from 50%, 75%, 85%, 90%, 95–100%, the composites underwent a series of change from green, olive, brown, orange, dark-red to transparent, respectively, taking a few seconds ($t < 10$ s) in every humidity change. Therefore, it is an appropriate component for rubber-based sensor to endow sensor with humidity response. However, the prepared materials still cannot be effectively conducting under a low relative humidity (RH) due to the weak conductivity of natural polymer, limiting further application of rubber-based sensor^{2, 13}. Incorporation of conductive filler, such as carbon nanotubes, graphene and metal, is an effective method to improve the conductivity under a low RH, assistance with respond to external stimuli¹⁴. Especially, during rubber latex film-formation process, a primitive successive pathway is self-assembly by two-dimensional conductive filler (e.g. WS₂ nanosheet¹⁵, Ti₃C₂ MXenes^{9, 16}, graphene¹⁷) based on the volume exclusion effect of rubber particles. For example, Guo et al. used two-dimensional Ti₃C₂ MXenes and epoxidized natural rubber (ENR) latex to prepare self-healable elastomer for intelligent sensing¹⁶. Therefore, combination of conductive filler and natural polymer enables the rubber-based sensor to achieve strain and humidity sensing simultaneously.

Metal nanoparticles (e.g. Ag, Au nanoparticles) are frequently used for conductive fillers as well as significant applications in photothermal conversion¹⁸. Differing from common heating method, the heat of metal nanoparticles can be localized in a submicrometer size by the photothermal conversion, which arouses intense interest in practical applications. Cao et al. fabricated a tannic acid antibacterial hydrogel with photothermal enhanced anti-infective therapy by incorporation of Ag nanoparticles (Ag NPs)¹⁹. Upon infrared illumination, the hydrogel exhibited a stronger anti-infective behavior on the mice's wound, which completely healed and became smooth in 7 days compared with control groups. Nie et al. added the Ag NPs into cotton textiles to obtain a self-disinfecting function by light-driven²⁰. Under 532-nm light illumination, the bacteria can be effectively eliminated. Despite brilliant achievements, little effort in photothermal sensor was reported by incorporation Ag NPs so far.

Based on the above understanding, in this paper, we aimed to fabricate a multifunctional rubber-based sensor (MRFS) with multiple responses to infrared, temperature, humidity and strain by using XSBR latex, carboxymethyl starch sodium (CMS) and AgNO₃. Firstly, the aldehyde-modified carboxymethyl starch

sodium (ACMS) with a humidity response was prepared. Benefiting from the flexible and elastic matrix, ACMS effectively overcame the disadvantage, e.g. brittleness and a low elongation at break ($\epsilon < 10\%$). Then it served as reducing agent to prepare the Ag NPs and Ag nanoflakes (Ag NFs). During latex film-formation process, Ag NPs were uniformly dispersed in the rubber matrix; meanwhile, a successive leaf-vein-like Ag network was formed by the two-dimensional Ag NFs stacking based on the volume exclusion effect of rubber particles. The Ag NPs had the function of photothermal effect; simultaneously the successive Ag NFs improved the conductivity of the MRFS due to the formation of conductive pathway. Under infrared irradiation, the resistance and temperature of MRFS changed rapidly. Based on these performances, infrared proximity sensor and temperature sensor were fabricated to sense the human proximity and monitor body temperature. Additionally, owing to the hydrophilicity of ACMS, the MRFS exhibited an ability of humidity sensing so that a respiratory detection device was designed. Furthermore, benefiting from the elastic matrix, the MRFS can also be used for strain sensing. Finally, similarly with human skin, as a wearable and flexible sensor, MRFS shows an effective antibacterial property to protect internal tissues from the invasion of harmful bacteria owing to the antibacterial activity of nanosilver.

2. Results And Discussion

2.1 Structure and properties of MRFS

The Experimental section containing Materials, Preparation and Characterization is provided in Supporting Information. The synthesis and characterization of ACMS is shown in Figure S1 to S5 (Supporting Information). To better understand the fabrication of MRFS, we conducted a preliminary experiment to prepare XSBR/CMS films without nanosilver. The details of the preparation, structure and properties of XSBR/CMS films please find in Supporting Information (Figure S6 to S9). As for the fabrication of MRFS, the ACMS containing aldehyde groups serve as reducing agent for preparation of Ag NPs and Ag NFs. The preparation method of Ag NPs and Ag NFs solution are displayed in Supporting Information. Once the $[\text{Ag}(\text{NH}_3)_2]^+$ solution was added dropwise into the ACMS solution, the colorless ACMS solution changed into yellow immediately, indicating the formation of nanosilver, as shown in Figure 1a. The reaction mechanism between ACMS and $[\text{Ag}(\text{NH}_3)_2]^+$ is shown in Figure S10 (Supporting Information). In the UV-Vis spectra, a new absorption peak appears at 413 nm belongs to nanosilver, showing that the reduction reaction occurred successfully²¹. The XRD pattern of XSBR/ACMS film with 5 wt% nanosilver shows characteristic diffraction peaks of Ag at 38.2° , 44.4° , 64.7° , 77.7° and 81.0° (Figure S11, Supporting Information), which corresponds to the reflection planes of Ag (111), (200), (220), (311) and (222), respectively²². Furthermore, after the reaction between ACMS and $[\text{Ag}(\text{NH}_3)_2]^+$, a new peak appears at 1643 cm^{-1} in the FTIR spectra (Figure S12, Supporting Information), which is attributed to the asymmetric stretching vibration of carboxylate since that the aldehyde groups are transformed into carboxyl groups after the reaction²³. In our strategy, the polyvinyl pyrrolidone (PVP) was used to control the morphologies of reductive nanosilver, namely Ag NPs or Ag NFs²⁴. It is well known that PVP is a common protective agent in the preparation of Ag NPs, which effectively prevents the reductive Ag NPs

from agglomeration. As a result, with PVP, Ag NPs is the main product in our films, and only Ag NPs can be found on the cryo-fractured surface of the XSBR/ACMS film with 15 wt% Ag (Figure 1b). Contrariwise, the reductive nanosilver grows into Ag NFs with thickness of about 40 nm under action of ACMS without PVP, which is confirmed from the SEM image in Figure 1c. The above successful morphology control of reductive nanosilver in the film is the key to photothermal conversion and conductivity improvement of MRFS.

Figure 1d illustrates the preparation process of MRFS, and the details of preparation please find in Supporting Information. Ag NPs and Ag NFs with 30 wt% content are pre-prepared in ACMS solution with/without PVP, respectively. Then, the Ag NPs/ACMS and Ag NFs/ACMS solution with the same content of nanosilver are mixed with XSBR latex together. During the film-forming process, Ag NPs and Ag NFs are unable to enter the inside of latex particles. They are thus dispersed in the interstitial space between latex particles. With the continuous water evaporation, the activity space for the Ag NP and Ag NFs is limited further²⁵. Especially for the Ag NFs at a higher content of 20-30 wt%, the reduction of the interstitial volume forces the Ag NFs stacking spontaneously. Subsequently, the latex particles are close-packed and slowly deform under the capillary force which originates from reduced interstitial “channels” by water transfer to the surface for evaporation²⁶. Meanwhile, the Ag NFs and Ag NPs are confined absolutely in the interstices of the coagulated XSBR particles. As a result, benefiting from the volume exclusion effect²⁷, a “leaf-veins-like” network is formed by the two-dimensional Ag NFs stacking (Figure 1e). Similar results have been reported by Zhang et al. They developed ultrathin two-dimensional WS₂¹⁵, CNT⁸ and Ti₃C₂ MXenes¹⁶ to construct segregated network structure by the similar film-forming process. When the size of two-dimensional filler is close to that of latex particles, the particles will be separated by the filler one by one. However, in our system, because abundant Ag⁺ is reduced, the size of Ag NFs is too larger (with an average length of > 9.7 μm) to separate the XSBR particles (average size at ~ 200 nm) one by one. As a result, a “leaf-vein-like” network, differing to the segregated network structure reported by Zhang et al., is constructed as conductive pathway in the rubber matrix, improving the conductivity of MRFS. At the same time, the XSBR matrix endows the MRFS with excellent flexibility that it can be distorted, stretched and bended (Figure 1d). The details of the leaf-vein-like structure can be observed in Figure 1f~ h. The SEM image with low magnification (2600 ×) (Figure 1e) shows that the leaf-vein-like structure is throughout the whole rubber film. Meanwhile, a great number of particles with a size of about 250 nm is dispersed uniformly in the space separated by Ag NFs “veins” (Figure 1g and 1h)²⁸, which was confirmed as Ag NPs (Figure S13, S14, S15 and Table S1, Supporting Information). Similar structure also can be found in the MRFS-25 (Figure S16, Supporting Information). The magnified view in Figure 1h (20000 ×) strongly confirms that the nanosilver “veins” are composed of stacked Ag NFs (white dash line). The equilibrium swelling experiment of MRFS provided additional information about the formation of Ag NFs leaf-vein-like networks. The swelling ratio of MRFS (Figure S17, Supporting Information) decreased from 396% of MRFS-5 to 297% of MRFS-30 due to the restriction effect of leaf-vein-like networks on the XSBR matrix. In addition, the morphologies of MRFS-5, 10 and 20 are also shown in Figure S18 (Supporting Information), which confirms the morphological evolution of reduced nanosilver

from Ag NFs and to leaf-vein-like structure. The fine dispersion of ACMS was discussed in Figure S19 (Supporting Information), which endows the MRFS with a high sensitivity to the moisture in the air (will be discussed below).

The hydrophilicity of MRFS was evaluated by the contact angle with deionized water²⁹. Figure 2a shows that the contact angle decreases from 45.9° of the MRFS-5 to 17.9° of the MRFS-30. It should be mentioned that the content of ACMS is identical in all the samples of MRFS (20 wt%). Therefore, the more content of nanosilver with high surface energy in MRFS should be a reason for the decreased contact angle. Especially, the contact angle sharply decreases from 36.6° of the MRFS-20 to 17.9° of the MRFS-30, which suggests that the formation of successive Ag NFs network further improves the hydrophilicity of MRFS, being advantageous to humidity sensing. The evolution of water content for samples tested under 75% RH as a function of time is shown in Figure 2b¹⁰. The water content for all of the samples increases until achieves an equilibrium state. In the first 10 min, the water content is almost identical for all samples, predominantly because the ACMS with the same content play a main role at the beginning of water absorption. For all of the samples, with the nanosilver content increasing, the water content increases accordingly. For example, it increases from 2.8% of the MRFS-5 to 20.2% of the MRFS-30 at 430 min, attributing to the high surface energy of more nanosilver. In summary, ACMS and nanosilver play pivotal roles in the hydrophilicity improvement.

Typical stress-strain curves of MRFS tested at 70% ambient RH are plotted in Figure 2c. Contrary to general nanocomposites, the mechanical properties are not improved by nanosilver, and the samples have instead weaker mechanical properties³⁰. With increasing content of Ag, the tensile strength decreases from 7.98 MPa of the MRFS-5 to 5.66 MPa of the MRFS-30. Correspondingly, the Young's modulus decreases from 37.76 MPa to 9.30 MPa (Figure 2d). Combined with the foregoing results, the ambient moisture is absorbed rapidly by the MRFS and then diffuses into the inside of the samples, serving as plasticizer in the materials³¹. In addition, for the sample of MRFS-30, the weakened mechanical properties are more obvious with the extension of time at an ambient humidity as shown in Figure 2e. Only 4 min at the 70% RH, the tensile strength and elongation at break sharply decreases from 5.66 MPa and 367% to 3.65 MPa and 310%, respectively, due to the excellent water adsorption. Conversely, there is little change in mechanical properties for the MRFS-10 with time (Figure S20, Supporting Information). Although the MRFS-30 shows the weakened mechanical properties, the tensile strength and elongation at break still maintain > 3.5 MPa and > 300%, respectively, which is competent for most practical applications as flexible sensing device³².

Figure 2f shows the conductivity of MRFS as a function of nanosilver content at ambient RH (~ 70%). The neat XSBR and MRFS-5 show a much low conductivity of 10^{-11} S/m and 10^{-8} S/m, respectively. When the nanosilver content increases to 10 wt%, the conductivity of MRFS-10 increases sharply from 10^{-8} S/m up to 10^{-4} S/m. The conductivity further increases to 0.010 S/m for the MRFS-20. It is well known that the conductive filler can form a network leading to a sudden rise of the conductivity for the composites at a certain loading which is known as the percolation threshold (ϕ_c). ϕ_c can be expressed as

follows, $\sigma_c = \sigma_f[(\phi - \phi_c)/(1 - \phi_c)]^t$, where σ_c , σ_f , ϕ and t are conductivity of samples, conductivity of the filler, content of filler and critical exponent, respectively. According to the equation, ϕ_c is calculated to be 9.97 wt% which is close to the nanosilver content in the MRFS-10. Consistent with the calculation results, the insets of Figure 2f shows the obvious conductivity in MRFS-10. The low percolation threshold is attributed to the formation of Ag NFs (Figure S18b) connected with Ag NPs to form conductive pathways³³. As expected, the MRFS-30 shows the highest conductivity of 0.0550 S/m due to the formation of “leaf-vein-like” conductive pathway at higher nanosilver content. Therefore, MRFS-30 was selected as the most suitable candidate to fabricate the sensor because of the best conductivity and outstanding hydrophilicity.

2.2 Infrared and temperature sensing of MRFS based on the photothermal effect

Benefiting from the Ag NPs, the MRFS exhibits obvious photothermal effect³⁴. The MRFS-30 shows a high selectivity to the near infrared (NIR) irradiation with wavelength at 808 nm and its resistance decreased rapidly once being irradiated by a NIR with 808 nm wavelength (Movie S1, Supporting Information). The ultraviolet and natural light have no effect on the MRFS-30. Figure 3a shows the resistance changes of the MRFS-30 which is irradiated by the NIR (808 nm) under different power (0.14, 0.27, 0.41 W/cm²), distance (30, 15, 5 cm) and time (3, 6, 9 s). With the variables monotonic increasing or decreasing, the electrical signal of $(R-R_0)/R_0$ has corresponding changes. For example, under the irradiation power of 0.14 W/cm², the value of $(R-R_0)/R_0$ is -0.035 and then decreased to -0.279 under the irradiation power of 0.41 W/cm². To find the reason of resistance decreasing under NIR irradiation, the real-time change of resistance was recorded by a 7-digit digital multimeter (DMM 7510, Keithley, America) as the MRFS-30 was continuously illuminated; simultaneously, its temperature was recorded by an infrared thermal imager (H16, Hikmicro, China) to evaluate the photothermal effect of material. As shown in Figure 3b, the $(R-R_0)/R_0$ only takes 20 s to reach the minimum value of -0.27 with a corresponding temperature increases from 28.6 up to 80.6 °C, showing an excellent NIR response. Then, with the irradiation time increases to 80 s, the $(R-R_0)/R_0$ increases from -0.27 to 0 while the temperature further raises to 107.1 °C. Similar phenomenon of resistance decreasing is also found in the MRFS-30 being heated. As shown in Figure 3c, when the MRFS-30 is heated from 28.7 to 48.1 °C, its $(R-R_0)/R_0$ decreases from 0 to -0.26 and then recovers to 0 when it was cooled to 34.6 °C. This implies that the resistance decreasing of the MRFS-30 is related to the temperature rather than NIR. It is well known that temperature increasing often leads to a resistance increasing for conventional metal materials³⁵, such as platinum³⁶ and silver.¹ However, in the MRFS-30, Ag NPs and Ag NFs serve as the main conductive medium which turn out a contrary result. The X-ray photoelectron spectroscopic (XPS) spectrum and SEM image solved the conundrum as shown in Figure 3d and 3e. Figure 3d evaluates the ionic states of Ag element. The two main peaks of Ag 3d appear at 374.30 and 368.27 eV, which belong to 3d_{5/2} and 3d_{3/2}³⁷, respectively. For the peak of 3d_{3/2}, two peaks are further deconvoluted at 368.32 and 367.74 eV, which are consistent with the binding energy of Ag and Ag₂O, respectively^{38,39}. It is noteworthy that Ag₂O is a common

semiconductor with negative temperature coefficient, namely, resistance decreasing with temperature rising^{40, 41}. As for the MRFS, in fact, the ACMS with substitution degree of 2.8% (calculated by the integral of peak areas from H-NMR) cannot enable all the Ag (I) to be completely reduced in the MRFS-30. Therefore, during the film-formation process, partial Ag₂O is formed on the surface of rubber film when it contacts with air. The cubic Ag₂O with the size at 1 μm can be seen on the top surface of MRFS-30 from the SEM image in Figure 3e^{42, 43}. After soaked by ammonia solution, the Ag₂O was dissolved, causing a bumpy surface (Figure S21, Supporting Information)⁴⁴. As a result, the resistance of soaked MRFS-30 without Ag₂O no longer decreases with risen temperature but increases with irradiation time from 0 to 2.83 during 70 s (Figure 3f). Contrarily, the untreated MRFS-30 shows a resistance decrease once being irradiated under NIR irradiation. In summary⁴⁵, upon NIR irradiation, the nanosilver strongly absorb NIR, inducing electrons transition to an excited state. At subpicosecond timescales, the electrons scatter, leading to the redistribution of hot electrons. Subsequently, the heat is transferred to metal lattice by the electron-phonon coupling, then the temperature of MRFS-30 rises, leading to the resistance decreasing due to the existence of Ag₂O. When the temperature rises to a certain extent (~80 °C), metallic nanosilver plays dominant roles in determining the resistance, which causes a continuous increase in the resistance of the MRFS-30.

Based on the sensitive sensing of MRFS-30, we designed infrared sensors as shown in Figure 3g and 3h. In Figure 3g, we fabricated an infrared proximity sensor which senses the light reflected by the human body (human hand) irradiation from an external infrared source (0.41 W/cm²)⁴⁶. While the hand closes to the infrared source, the reflected light causes the values of $(R-R_0)/R_0$ correspondingly descending from 0 to -0.038 during 7.4 s; additionally, with the hand away, no infrared is reflected on the surface of infrared proximity sensor, leading to the $(R-R_0)/R_0$ increasing accordingly. Furthermore, we tested the sensing of MRFS-30 for various materials (paper, human hand, rubber glove and iron). Owing to the different roughness on the surface, the minimal $(R-R_0)/R_0$ shows discernible difference during the same time. For example, the minimal values are -0.030, -0.038, -0.051 and -0.061 for paper, hand, glove and iron, respectively, showing a fine sensitivity of MRFS-30. Therefore, the MRFS-30 has a potential application to alarm system to prevent thieves from invading and distinguish the intruder. In Figure 3h, the infrared sensor is worn on the blind person body for alarm of proximity danger area which equip a NIR source. As the blind person close to the danger area (construction site, road, abandoned building and so on) at $t = 20$ s, the buzzer was alarming and $(R-R_0)/R_0$ sharply decreased from 0 to -0.10 to warn the blind person for danger, reminding him to leave here⁴⁷.

Subsequently, the photothermal effect of MRFS was further investigated. In Figure 4a, the neat XSBR and MRFS are illuminated by the 808 nm NIR with a distance of 10 cm and power at 0.54 W/cm². A series of MRFS with different nanosilver content shows an excellent photothermal effect. In 40 s, the temperature of MRFS sharply rises from room temperature to more than 100 °C. For example, the temperature of MRFS-30 rises from 24.9 to 143.4 °C in 40 s as shown in Figure 4b. Conversely, the temperature of pure XSBR is almost unchanged which has been maintained at ~25 °C. We also investigated the

photothermal effect of MRFS-30 under different power (Figure 4c). Especially, under a 0.82 W/cm² NIR irradiation, the temperature rises to 255.2 °C rapidly, which chars the paper on the back of the MRFS-30 (Figure S22, Supporting Information). When the NIR irradiation is turned off, the MRFS-30 only takes 102.4 s to cool down to the room temperature. To quantify the photothermal effect, the photothermal conversion efficiency (PCE, η) was calculated as following equation^{48, 49}:

$$\eta = \frac{hS(T_{Max} - T_{Surr}) - Q_0}{I}$$

1

Where h is the heat transfer coefficient (%); and S is the surface area (cm²) of beaker; and T_{Max} and T_{Surr} are the maximal temperature and surrounding temperature (room temperature: 25.1 °C), respectively; Q_0 is the heat yielded from the solar absorbed by the beaker and the water; I is the effective NIR power (W/cm²). The detailed method and calculation are shown in Supporting Information and Figure S23. As a result, the PCE of MRFS-30 is calculated as 78.6%, which is higher than most previously reported work (containing organic molecules, polymers, and inorganic materials.) for red or infrared light in recent (Table S2, Supporting Information).

Based on the flexibility, the MRFS-30 can be bended and folded into letter (A, J and N) and number (3, 6 and 8), as shown in Figure 4d. Under a 0.2 W/cm² NIR irradiation, the thermal images clearly distinguish the significant shapes. The photothermal effect of MRFS can further extend the application of shape memory materials in some scenarios without additional heat source. As shown in Figure 4e, the MRFS-30 is twined on the surface of a shape memory alloy (SMA, transition temperature: ~60 °C) to endow it with photothermal response. This SMA has no photothermal conversion ability (Figure S24, Supporting Information). As seen, the permanent shape (heart-8, star and clip) of SMA can be simply recovered under NIR irradiation (Movie S2, Supporting Information).

To achieve temperature sensor application, we further investigated the correlation between temperature and resistance. Figure 4f shows the resistance changes at periodic temperature of 30 to 60 °C and 40 to 80 °C. Specifically, the MRFS-30 is heated to 60 °C by the NIR and then cooled to 30 °C spontaneously. After 400 s, it is heated to 80 °C and cooled to 40 °C. The resistance changes are collected by the 7-digit digital multimeter (DMM 7510, Keithley, America) simultaneously. Similarly, with the temperature rising and dropping, the $(R-R_0)/R_0$ decreases or increases between 0 at 30 °C and -0.13 at 60 °C, 0.04 at 40 °C and -0.25 at 80 °C, respectively. However, when the cyclic temperature rises at 90 °C and 130 °C, contrary results are shown in Figure 4g because the more Ag NPs and Ag NFs play dominant roles in influencing the resistance. The risen temperature causes the decreasing of $(R-R_0)/R_0$ from 0 at 90 °C to 1.22 at 130 °C. According to the unique temperature-resistance response, we investigated the $(R-R_0)/R_0$ changes from room temperature to 107 °C as shown in Figure 4h and the temperature coefficient of resistance (TCR) is quantified as follows⁷:

$$TCR = \frac{(R - R_0)}{R_0} \cdot \frac{1}{\Delta T} \times 100\%$$

2

Where the ΔT is the temperature change. In Figure 4h, the three linear relationship between $(R-R_0)/R_0$ and temperature can be found. Therefore, three TCRs are obtained: -2.064%/°C (28.9~ 33.6 °C), -0.3861%/°C (33.6~ 71.5 °C) and 1.616%/°C (92.2~ 107.0 °C). Compared with the other temperature sensor in recent reports (Table S3, Supporting Information), the MRFS-30 shows a more sensitive temperature response due to the high TCR.

Benefiting from the wide linear range (33.6~ 71.5 °C) and outstanding linear relationship, a temperature sensor is fabricated by MRFS-30 to monitor the changes in the temperature range. Especially, the temperature variation range of human body is just within the foregoing range, which is instrumental in monitoring body temperature⁵⁰. Therefore, we designed a wearable body temperature sensor by using the MRFS-30 as shown in Figure 4i. To avoid the influence of skin humidity, the sensor was sealed by sellotape and was worn on the surface of arm skin. In Figure 4j, the body temperature is 34.4 °C with $(R-R_0)/R_0$ at 0. Rapidly, the $(R-R_0)/R_0$ decreases from 0 to -0.12 during 0.5 s (Figure 4k) with the heat source (hot water at 46.3 °C) contact with the arm skin. As seen, the temperature sensor shows an excellent signal stability. In Figure 4l, the $(R-R_0)/R_0$ is retained at 0 during 60 s at room temperature. Then it decreases and keeps at -0.4 during the same time when the sensor is worn on the arm skin, showing a temperature of 33.3 °C (Figure 4m). Since the person has a “fever” (skin temperature: 35.6 °C), the signal decreases and steadies at -0.46 (Figure 4n).

2.3 Humidity sensing of MRFS

Figure 5a shows the changes of conductivity of MRFS at various RHs, and the values of conductivity are summarized in Table S4 (Supporting Information). At the lowest test 33% RH, although the conductivities of the three samples seem to be close to each other, the conductivity of MRFS-30 is about 56.6 times (5.56×10^{-3} S/m) that of MRFS-5 (9.82×10^{-5} S/m). This gap is further widened in higher RHs. For example, the MRFS-30 exhibits the most distinct response to the humidity and its conductivity changes from 0.00556 S/m at 33% RH to 0.147 S/m at 93% RH almost 26 times. Simultaneously, the MRFS-30 owns the highest conductivity due to the successive nanosilver network and highest Ag content. This suggests that the MRFS-30 can find suitable application in humidity-responsive device⁵¹. Table S5 displays the conductivity of the rubber conductive sensor with only 30 wt% Ag NPs, suggesting that the conductivity is improved by the Ag NFs.

The continuous data collection of resistance was conducted by a 7-digit digital multimeter (DMM 7510, Keithley, America) in a RH continuously increased from 33–57%, 75% and 93% in sequence, as shown in Figure 5b. The sample of MRFS-30 was taken out from an oven in which the RH was ~ 25%, and then it was cut into rectangle with 10×30×0.3 mm immediately. However, during this very short process, the sample still absorbed a small amount of moisture from the air (RH≈ 70%). When it is placed at 33% RH,

the small amount of moisture is lost, which make the $(R-R_0)/R_0$ increase slowly from 0 to 0.1207 during the first 2100 s at 33% RH (see Figure 5b). When the RH increases from 33–57%, the $(R-R_0)/R_0$ sharply decreases from 0.1207 to 0.1196 during the first 0.5 s (inset in Figure 5b, the minimal time interval for data collection of the 7-digit digital multimeter is 0.5 s). This sharply decrease in resistance lasted 316 s until the value reached a relative stable stage. Similar situation can be found when the RH changes once again from 57–75%. The $(R-R_0)/R_0$ obviously decreases from -0.4404 to -0.4427 during 0.49 s (Figure S25, Supporting Information), exhibiting a highly sensitive humidity response. Due to place in the 75% RH for long time (~3300 s), the MRFS-30 ceaselessly absorbs moisture until saturation, which showed no significant change when it is transferred into a 93% RH. The picture of saturated MRFS-30 was shown in Figure S26 (Supporting Information), from which water droplets can be clearly seen on the sample's surface. In addition, the brightness of LED is of course stronger with the RH increasing due to the resistance reduction. Subsequently, we recorded the change of $(R-R_0)/R_0$ in successively decreased RH from 93%, 75%, 57–33%, as shown in Figure 5c. In this case, another sample of MRFS-30 is first pre-placed at a 93% RH until the $(R-R_0)/R_0$ did not change. Similarly, the $(R-R_0)/R_0$ significantly increases with the change under ambient humidity. For example, the $(R-R_0)/R_0$ increases from 0 at 93% RH to 0.0148 at 75% RH during the first 1.23 s in Figure S27 (Supporting Information). However, because the water loss rate is much greater than water absorption rate, the $(R-R_0)/R_0$ continuous increases from 0.005 to 0.091 at the 57% RH and from 0.091 to 0.952 at 33% RH, respectively (Figure 5c).

We compared the response humidity sensitivity of the MRFS-30 with an electronic hygrometer (AR807, Smart Sensor, China). As shown in Figure 5d and 5e, the MRFS-30 exhibits a more sensitive response than the electronic hygrometer in a short period of time. For example, it takes 78 s for the electronic hygrometer to increase the humidity value from 25–26% when it is placed in ambient humidity (~ 60% RH) from a 50 °C oven with 25% RH (Movie S3, Supporting Information, see the data on the screen). It takes 1984 s to arrive the ambient humidity (~ 58%). However, the time of response to humidity change for MRFS-30 is only 1 s and achieves the ambient humidity only needed 134 s (Movie S4, Supporting Information, see the data on the screen). Additionally, to the best of our knowledge, most of reported humidity sensors is based on inorganic material or natural polymer (cellulose, silk and so on) so that they are brittle with low elongation at break, limiting the application in flexible and stretchable sensor. Herein, we compare the time of response to the humidity change and elongation at break by many works in recent years (detailed information shown in Figure S28 and Table S6). In short, the MRFS-30 shows the better comprehensive capacity with rapid response and large elongation at break, which is instrumental in a wide application.

Figure 5f shows the humidity response of MRFS-30 at alternating high RH and low RH (interval residence time was 120 s). Consistent with the foregoing results, when the sample was placed in a higher humidity (57%), the $(R-R_0)/R_0$ decreased; otherwise, it increased. In addition, the larger humidity difference, the more obvious value of $(R-R_0)/R_0$ is shown, indicating that the MRFS-30 is sensitive for the humidity change. Based on these performances, we evaluated the prospect of MRFS-30 serving as a core element of humidity sensor. It is well known that water in the human body is excreted continually through skin

evaporation and breathing⁵². Therefore, there is small amount of moisture on fingers. We fixed the MRFS-30 on a non-conductive hard plastic to test its response to touching. When the MRFS-30 was touched by finger, the $(R-R_0)/R_0$ decreased accordingly (Figure 5g). Compared with ambient humidity change, the decrease is quite small that the $(R-R_0)/R_0$ only changed from 0 to -0.07, showing a low detection limit and high sensitivity. When a rubber glove is worn to prevent the moisture diffusion onto the MRFS-30, the resistance no longer changes, which confirms that the resistance change does not originate from the pressure (Movie S5, Supporting Information). Similar response to blowing is recorded in Figure 5g⁵³. As soon as the moisture of blowing contacted the MRFS-30, the $(R-R_0)/R_0$ rapidly reduced. When we stopped blowing, the $(R-R_0)/R_0$ increased again.

Based on above results, we designed a respiratory detection device through connecting the MRFS-30 with a mask and software (Figure 6a) to monitor the patient's physical condition³². When the patient's health is in crisis, reflecting in breathing with uneven intervals, the software records the abnormal breathing to draw caregiver's attention and takes the next first aid measures. To address this, the respiratory detection device was firstly used for monitoring a normal breathing as shown in Figure 6b. Although the trend of $(R-R_0)/R_0$ is decreasing (from 0 to -0.56) owing to the stronger water adsorption, it can be controllable to balance the water adsorption and loss. For example, after 400 s, the resistance change is stable, and the respiratory interval is 2.9 s at $t=420$ s and 430 s (Figure 6b). While the experimenter takes deep breathings, the interval increases to 4.5 s at $t=50$ s and 83 s (Figure 6c). These results show a respiratory status of healthy people with steady respiratory intervals. According to these results, a respiratory detection device was designed to monitor patient's breathing (Figure 6d). Figure 6e shows the respiratory condition including healthy and dangerous breathing. In healthy breathing, the constant intervals of breathing are seen with 2.9 s. In addition, there is dangerous situation in the red zone. The zone I, II and VI represent the sudden cessation of breathing for duration of 8.6 s, 14.9 s and 20.3 s, respectively; the zone III and V stand for the condition that patient can only exhale but not inhale for duration of 22.5 s and 13.1 s, respectively; and the zone IV represents abnormal breathing for duration of 20.7 s, which implies the duration of the patient in crisis. The real-time breathing recording is instrumental in making accurate judgment for doctor and timely handling the situation in an emergency (such as at home or outdoor). In addition, the respiratory monitoring can be conducted by the wireless connection with smartphone, achieving a remote monitoring (Figure 6f). Furthermore, the MRFS-30 can be used to monitor the bodily perspiration by the wireless connection with smartphone as shown in Figure 6g. Once the water molecules of perspiration diffuse on the surface of MRFS-30, the $(R-R_0)/R_0$ sharply decreases from 0.09 to -0.57 for 57 s. As the MRFS-30 is made into a humidity alarm device, wireless connection with smartphone, the phone will give an alarm music once the $(R-R_0)/R_0$ decreases below the preset threshold. This can timely inform the caregiver to care for patients to improve their quality of life⁵⁴.

2.4 Strain sensing of MRFS

We also expanded the potential application of MRFS for strain sensing, benefiting from the elastic rubber matrix. To avoid the influence of humidity on the strain sensing, we placed the MRFS-30 at the ambient

humidity (~ 60%) until the resistance was constant. The MRFS was connected to a 7-digit digital multimeter (DMM 7510, Keithley, America) to gauge the resistance; meanwhile, a tensile machine (U-CAN UT-2080, Taiwan, China) was set at a constant stretching rate. The schematic diagram of the strain sensing experimental setup is exhibited in Figure S29 (Supporting Information). Figure 7a shows the resistance change of MRFS-10, 20 and 30 with the strain increasing. The three samples have an excellent linearity (dash line). The slopes in Figure 7a, namely the gauge factors ($GF = \Delta[(R-R_0)/R_0]/\Delta\varepsilon$), are 0.527, 0.112 and 0.204 for the MRFS-10, 20 and 30, respectively. This result indicates that the MRFS have a stable GF in the strain range from 0 to 150%. Herein, we selected the MRFS-30 with better conductivity and higher GF to conduct further research, namely MRFS-30. The stability of GF was further confirmed in Figure 7b that two stretching rates of 50 mm/min and 500 mm/min are applied on the test samples of MRFS-30. As seen, the two curves almost overlap with the same GF= 0.112, which shows excellent stability of GF for the MRFS-30 under different stretching rates. Figure 7c shows the cyclic $(R-R_0)/R_0$ change (from ~0.08 to ~0.02) by the cyclic stretching at 50 mm/min and 25% strain. Unfortunately, the $(R-R_0)/R_0$ does not return to the initial value ($(R-R_0)/R_0= 0$) due to the uncrosslinking state of XSBR matrix, causing a residual deformation²⁵. However, the accordant changes of $(R-R_0)/R_0$ in different circle suggest the fine repeatability of MRFS-30 in dynamic sensing. Finally, we show the application of MRFS-30 for monitoring joint movements, including finger, wrist, elbow and knee as depicted in Figure 7d, 7e, 7f and 7g, respectively⁵⁵. Take finger bending as an example (Figure 7d). When the angle of the bent finger continuously increases (from 0 to 180°) and decreases (from 180 to 0°), the $(R-R_0)/R_0$ increases (from 0 to 0.28) and decreases (from 0.28 to 0) correspondingly, presenting peaks-like and troughs-like feature. The similar results are shown in Figure 7e, 7f and 7g for wrist, elbow and knee.

Finally, similarly with human skin, the MRFS-30 shows an effective antibacterial property (Figure S30, Supporting Information). By the inhibition zone method⁵⁶, distinguishable bacteriostatic rings of 3.9 and 15.1 mm are seen from the Escherichia coli (*E. coli.*, Gram-negative bacteria) and Staphylococcus aureus (*S. aureus*, Gram-positive bacteria), respectively.

3. Conclusion

In summary, we fabricated a flexible wearable multifunctional sensor with multiple responses to infrared, temperature, humidity and stain by using XSBR latex, CMS and AgNO₃. Firstly, CMS was changed into water-soluble ACMS, which was used to reduce the AgNO₃. Under the morphology-control of PVP, Ag NPs and Ag NFs were generated. After the film-formation, the Ag NPs were uniformly dispersed in the XSBR matrix, and the Ag NFs stacked to form successive network with “leaf-vein-like” structure. Then, MRFS was successfully fabricated. The nanosilver endowed the MRFS with photothermal effect (PCE of 78.6%) and outstanding temperature response (TCR of 2.046%/°C). Furthermore, the MRFS owned a high selectivity to the NIR with wavelength at 808 nm. Based on above, the infrared proximity sensor and temperature sensor were fabricated. For infrared proximity sensor, MRFS could be design as a wearable blind guiding device and distinguished signals from different materials, such as paper, hand, glove and iron. For temperature sensor, MRFS could be used for monitoring human body temperature, which

exhibited a rapid sensing of only 0.5 s for temperature changes. Owing to the excellent hydrophilicity of ACMS and nanosilver, MRFS found application in the humidity sensor was designed, which has a rapid RH response during the first 0.5 s for the RH change and a low detection limit ($(R-R_0)/R_0 = -0.07$) for small amount of moisture on human skin. According to the outstanding performance, a respiratory detection device can be applied to monitor human breathing. Furthermore, benefiting from the elastic rubber matrix, the MRFS also serve as strain sensor to accurately monitor the motion of finger, wrist, elbow and knee. At last, MRFS exhibited an effective antibacterial property for *E. coli* and *S. aureus*.

Declarations

Supporting Information

Supporting Information is available from the Wiley Online Library or from the author.

Acknowledgements

This work was supported by the National Natural Science Foundation of China (22175044).

Author contributions

Supervision and design of the experiments: Zhongjie Zheng; Investigation: Zhongjie Zheng; Synteruptor software development: Li Yang

Writing—Original draft: Zhongjie Zheng.; Writing—Reviewing and Editing: Zhongjie Zheng, Chanhui Xu, Li Yang, Yunpeng Yang; Funding acquisition: Chuanhui Xu, Baofeng Lin, Lihua Fu.

Competing interests

The authors declare no competing interests

References

1. Zou, Z. Zhu, C. Li, Y. Lei, X. Zhang, W. Xiao, J. Rehealable, fully recyclable, and malleable electronic skin enabled by dynamic covalent thermoset nanocomposite. *Sci. Adv.* **4**, eaaq0508 (2018).
2. Wang, X. *et al.* Conductivity controllable rubber films: response to humidity based on a bio-based continuous segregated cell network. *J. Mater. Chem. A* **9**, 8749–8760 (2021).
3. Fan, J. Huang, J. Gong, Z. Cao, L. Chen, Y. Toward Robust, Tough, Self-Healable Supramolecular Elastomers for Potential Application in Flexible Substrates. *ACS Appl. Mater. Inter.* **13**, 1135–1144 (2021).
4. Dong, X. Cao, L. Si, Y. Ding, B. Deng, H. Cellular Structured CNTs@SiO₂ Nanofibrous Aerogels with Vertically Aligned Vessels for Salt-Resistant Solar Desalination. *Adv Mater* **32**, 1908269 (2020).

5. Xu, L. *et al.* Coolmax/graphene-oxide functionalized textile humidity sensor with ultrafast response for human activities monitoring. *Chem. Eng. J.* **412**, 128639 (2021).
6. Liu, LX. Chen, W. Zhang, HB. Wang, QW. Guan, F. Yu, ZZ. Flexible and Multifunctional Silk Textiles with Biomimetic Leaf-Like MXene/Silver Nanowire Nanostructures for Electromagnetic Interference Shielding, Humidity Monitoring, and Self-Derived Hydrophobicity. *Adv. Funct. Mater.* **29**, 1905197 (2019).
7. Lin, M. *et al.* A High-Performance, Sensitive, Wearable Multifunctional Sensor Based on Rubber/CNT for Human Motion and Skin Temperature Detection. *Adv Mater*, 2107309 (2021).
8. Liu, X. *et al.* Hierarchically Structured Self-Healing Sensors with Tunable Positive/Negative Piezoresistivity. *Adv. Funct. Mater.* **28**, 1706658 (2018).
9. Zhao, X. *et al.* Smart Ti₃C₂T_x MXene Fabric with Fast Humidity Response and Joule Heating for Healthcare and Medical Therapy Applications. *ACS Nano* **14**, 8793–8805 (2020).
10. Yu, P. He, H. Luo, Y. Jia, D. Dufresne, A. Reinforcement of Natural Rubber: The Use of in Situ Regenerated Cellulose from Alkaline–Urea–Aqueous System. *Macromolecules* **50**, 7211–7221 (2017).
11. Li, X. Liu, J. Li, D. Huang, S. Huang, K. Zhang, X. Bioinspired Multi-Stimuli Responsive Actuators with Synergistic Color- and Morphing-Change Abilities. *Adv. Sci.* **8**, 2101295 (2021).
12. Yao, K. Meng, Q. Bulone, V. Zhou, Q. Flexible and Responsive Chiral Nematic Cellulose Nanocrystal/Poly(ethylene glycol) Composite Films with Uniform and Tunable Structural Color. *Adv. Mater.* **29**, 1701323 (2017).
13. Xu, C. Wu, W. Zheng, Z. Nie, J. Chen, Y. Strengthened, conductivity-tunable, and low solvent-sensitive flexible conductive rubber films with a Zn²⁺-crosslinked one-body segregated network. *Composites Science and Technology* **203**, 108606 (2021).
14. Li, Z. *et al.* Asymmetrically Patterned Cellulose Nanofibers/Graphene Oxide Composite Film for Humidity Sensing and Moist-Induced Electricity Generation. *ACS Appl. Mater. Inter.* **12**, 55205–55214 (2020).
15. Wang, Y. Huang, X. Zhang, X. Ultrarobust, tough and highly stretchable self-healing materials based on cartilage-inspired noncovalent assembly nanostructure. *Nat. Commun.* **12**, 1291 (2021).
16. Guo, Q. *et al.* Protein-Inspired Self-Healable Ti₃C₂ MXenes/Rubber-Based Supramolecular Elastomer for Intelligent Sensing. *ACS Nano* **14**, 2788–2797 (2020).
17. Wei, S. Qiu, X. An, J. Chen, Z. Zhang, X. Highly sensitive, flexible, green synthesized graphene/biomass aerogels for pressure sensing application. *Compos. Sci. Technol.* **207**, 108730 (2021).
18. Ding, C. Huang, Y. Shen, Z. Chen, X. Synthesis and Bioapplications of Ag₂S Quantum Dots with Near-Infrared Fluorescence. *Adv. Mater.* **33**, 2007768 (2021).
19. Cao, C. *et al.* Biodegradable hydrogel with thermo-response and hemostatic effect for photothermal enhanced anti-infective therapy. *Nano Today* **39**, 101165 (2021).

20. Nie, X. *et al.* Light-driven self-disinfecting textiles functionalized by PCN-224 and Ag nanoparticles. *J. Hazard. Mater.* **416**, 125786 (2021).
21. Bastús, NG. Merkoçi, F. Piella, J. Puntès, V. Synthesis of Highly Monodisperse Citrate-Stabilized Silver Nanoparticles of up to 200 nm: Kinetic Control and Catalytic Properties. *Chem. Mater.* **26**, 2836–2846 (2014).
22. Wu, Z. Huang, X. Li, YC. Xiao, H. Wang, X. Novel chitosan films with laponite immobilized Ag nanoparticles for active food packaging. *Carbohydr. Polym.* **199**, 210–218 (2018).
23. Li, S. *et al.* Self-healing hyaluronic acid hydrogels based on dynamic Schiff base linkages as biomaterials. *Carbohydr. Polym.* **250**, 116922 (2020).
24. Padmos, JD. Boudreau, RT. Weaver, DF. Zhang, P. Impact of protecting ligands on surface structure and antibacterial activity of silver nanoparticles. *Langmuir* **31**, 3745–3752 (2015).
25. Xu, C. *et al.* Strengthened, Antibacterial, and Conductive Flexible Film for Humidity and Strain Sensors. *ACS Appl. Mater. Inter.* **12**, 35482–35492 (2020).
26. Nie, J. Fan, J. Gong, Z. Xu, C. Chen, Y. Frame-structured and self-healing ENR-based nanocomposites for strain sensors. *Eur. Polym. J.* **154**, 110569 (2021).
27. Song, Q. Chen, B. Zhou, Z. Lu, C. Flexible, stretchable and magnetic Fe₃O₄@Ti₃C₂Tx/elastomer with supramolecular interfacial crosslinking for enhancing mechanical and electromagnetic interference shielding performance. *Sci. China Mater.* **64**, 1437–1448 (2021).
28. Abdollahi, M. Rahmatpour, A. Khoshniyat, AR. Effect of the carboxylic acid monomer type on the emulsifier-free emulsion copolymerization of styrene and butadiene. *J. Appl. Polym. Sci.* **106**, 828–836 (2007).
29. Choi, M. *et al.* Functionalized Polyurethane-Coated Fabric with High Breathability, Durability, Reusability, and Protection Ability. *Adv. Funct. Mater.* **31**, 2101511 (2021).
30. Sheiko, SS. Dobrynin, AV. Architectural Code for Rubber Elasticity: From Supersoft to Superfirm Materials. *Macromolecules* **52**, 7531–7546 (2019).
31. Syed, IH. Stratmann, P. Hempel, G. Klüppel, M. Saalwächter, K. Entanglements, Defects, and Inhomogeneities in Nitrile Butadiene Rubbers: Macroscopic versus Microscopic Properties. *Macromolecules* **49**, 9004–9016 (2016).
32. Wang, Q. Ling, S. Liang, X. Wang, H. Lu, H. Zhang, Y. Self-Healable Multifunctional Electronic Tattoos Based on Silk and Graphene. *Adv. Funct. Mater.* **29**, 1808695 (2019).
33. Tang, Z. Kang, H. Shen, Z. Guo, B. Zhang, L. Jia, D. Grafting of Polyester onto Graphene for Electrically and Thermally Conductive Composites. *Macromolecules* **45**, 3444–3451 (2012).
34. Ruiz, D. *et al.* Ag/Ag₂S Nanocrystals for High Sensitivity Near-Infrared Luminescence Nanothermometry. *Adv. Funct. Mater.* **27**, 1604629 (2017).
35. Joh, H. *et al.* Surface Design of Nanocrystals for High-Performance Multifunctional Sensors in Wearable and Attachable Electronics. *Chem. Mater.* **31**, 436–444 (2018).

36. Huang, J. *et al.* Stretchable and Heat-Resistant Protein-Based Electronic Skin for Human Thermoregulation. *Adv. Funct. Mater.* **30**, 1910547 (2020).
37. Li, W. *et al.* Physical and optical properties of sol-gel nano-silver doped silica film on glass substrate as a function of heat-treatment temperature. *J. Appl. Phys.* **93**, 9553–9561 (2003).
38. Zhang, W. Sharma, G. Kumar, A. Shekh, MI. Stadler, FJ. Fabrication and characterization of Ni/Ag/Zn trimetal oxide nanocomposites and its application in dopamine sensing. *Mater. Today Commun.* **29**, 102726 (2021).
39. Sant, SB. Gill, KS. Burrell, RE. The nature of chemical species in novel antimicrobial silver films deposited by magnetron sputtering. *Philos. Mag. A* **82**, 1115–1136 (2002).
40. Subrahmanyam, A., Barik, UK. Synthesis of P-type transparent conducting silver:indium oxide (AlO) thin films by reactive electron beam evaporation technique. *J. Phys. Chem. Solids* **66**, 817–822 (2005).
41. Li, S. Hu, S. Xu, K. Jiang, W. Hu, J. Liu, J. Excellent visible-light photocatalytic activity of p-type Ag₂O coated n-type Fe₂O₃ microspheres. *Mater. Lett.* **188**, 368–371 (2017).
42. Kim, M-J. Cho, Y-S. Park, S-H. Huh, Y-D. Facile Synthesis and Fine Morphological Tuning of Ag₂O. *Cryst. Growth Des.* **12**, 4180–4185 (2012).
43. Wang, G. *et al.* Controlled synthesis of Ag₂O microcrystals with facet-dependent photocatalytic activities. *J. Mater. Chem.* **22**, 21189 (2012).
44. Lyu, LM. Huang, MH. Formation of Ag₂S cages from polyhedral Ag₂O nanocrystals and their electrochemical properties. *Chem. Asian J.* **8**, 1847–1853 (2013).
45. Chen, J. Ye, Z. Yang, F. Yin, Y. Plasmonic Nanostructures for Photothermal Conversion. *Small Science* **1**, 2000055 (2021).
46. Kim, YR. *et al.* Infrared Proximity Sensors Based on Photo-Induced Tunneling in van der Waals Integration. *Adv. Funct. Mater.* **31**, 2100966 (2021).
47. Wang H, *et al.* Bioinspired Fluffy Fabric with In Situ Grown Carbon Nanotubes for Ultrasensitive Wearable Airflow Sensor. *Adv Mater* **32**, e1908214 (2020).
48. Zong, L. Li, M. Li, C. Intensifying solar-thermal harvest of low-dimension biologic nanostructures for electric power and solar desalination. *Nano Energy* **50**, 308–315 (2018).
49. Xi, D. *et al.* NIR Light-Driving Barrier-Free Group Rotation in Nanoparticles with an 88.3% Photothermal Conversion Efficiency for Photothermal Therapy. *Adv. Mater.* **32**, 1907855 (2020).
50. Trung, TQ. Dang, TML. Ramasundaram S, Toi PT, Park SY, Lee NE. A Stretchable Strain-Insensitive Temperature Sensor Based on Free-Standing Elastomeric Composite Fibers for On-Body Monitoring of Skin Temperature. *ACS Appl. Mater. Inter.* **11**, 2317–2327 (2019).
51. Wang, Y. *et al.* Dual Resistance and Impedance Investigation: Ultrasensitive and Stable Humidity Detection of Molybdenum Disulfide Nanosheet-Polyethylene Oxide Hybrids. *ACS Appl. Mater. Inter.* **13**, 25250–25259 (2021).

52. He, Y. *et al.* A Highly Sensitive, Reversible, and Bidirectional Humidity Actuator by Calcium Carbonate Ionic Oligomers Incorporated Poly(Vinylidene Fluoride). *Adv. Funct. Mater.* **31**, 2101291 (2021).
53. Shen, D. Xiao, M. Zou, G. Liu, L. Duley WW, Zhou YN. Self-Powered Wearable Electronics Based on Moisture Enabled Electricity Generation. *Adv. Mater.* **30**, 1705925 (2018).
54. Xu, K. *et al.* A Wearable Body Condition Sensor System with Wireless Feedback Alarm Functions. *Adv. Mater.* **33**, 2008701 (2021).
55. Park, H. *et al.* Dynamically Stretchable Supercapacitor for Powering an Integrated Biosensor in an All-in-One Textile System. *ACS Nano* **13**, 10469–10480 (2019).
56. Meng, X. Duan, C. Zhang, Y. Lu, W. Wang, W. Ni, Y. Corncob-supported Ag NPs@ ZIF-8 nanohybrids as multifunction biosorbents for wastewater remediation: Robust adsorption, catalysis and antibacterial activity. *Compos. Sci. Technol.* **200**, 108384 (2020).

Figures

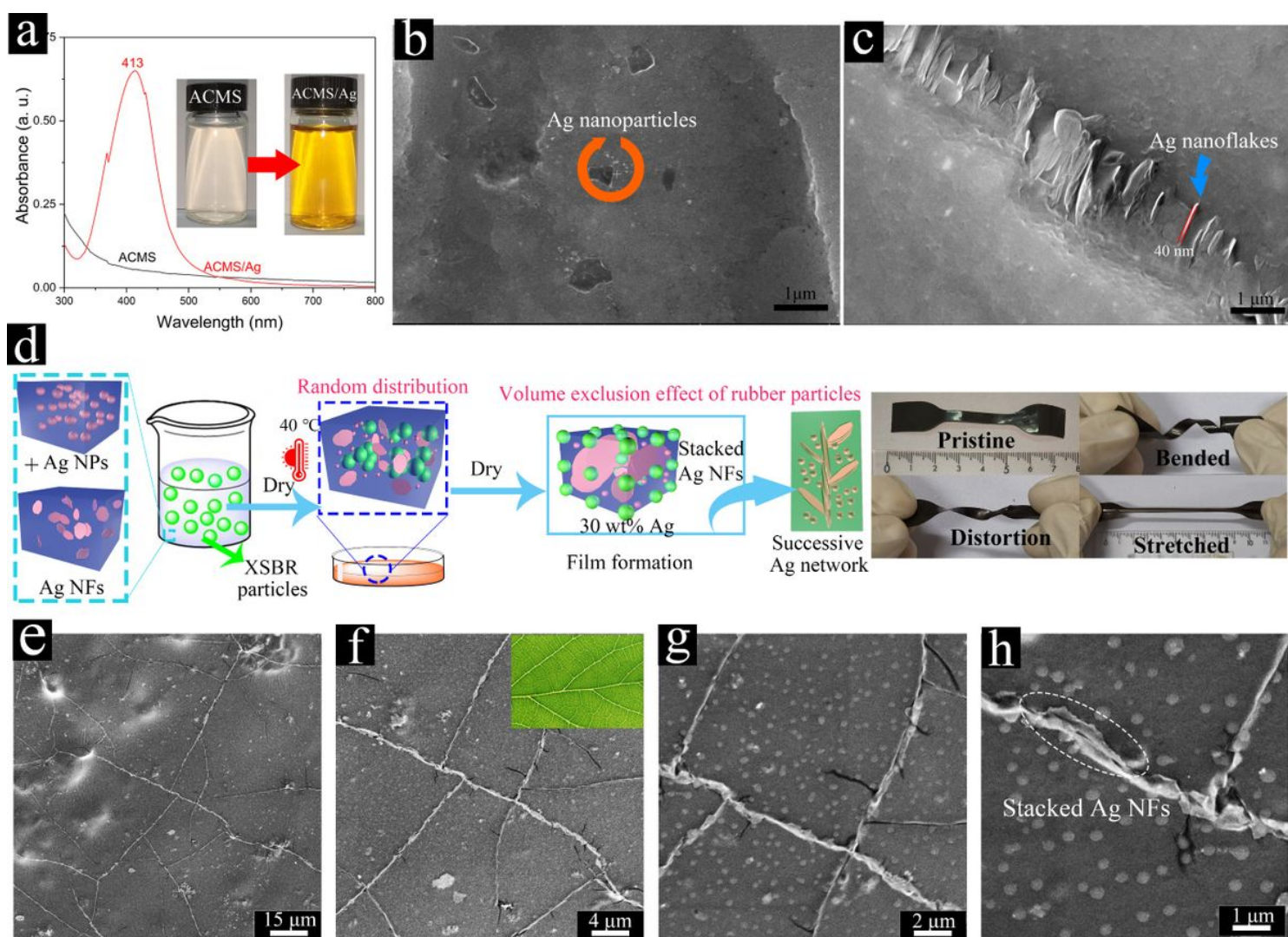


Figure 1

Characterization of nanosilver formation. (a) UV-Vis spectra of ACMS solution and ACMS/Ag solution. Insets show the color change with nanosilver formation. (b) and (c) control the morphology by PVP. Formation of Ag NPs with PVP (b), and formation of Ag NFs without PVP (c), containing 10 wt% nanosilver in the XSBR/ACMS film. (d) Fabrication process of MRFS-30. (e)~ (h) SEM images of cryo-fractured surface of MRFS-30 in different magnification.

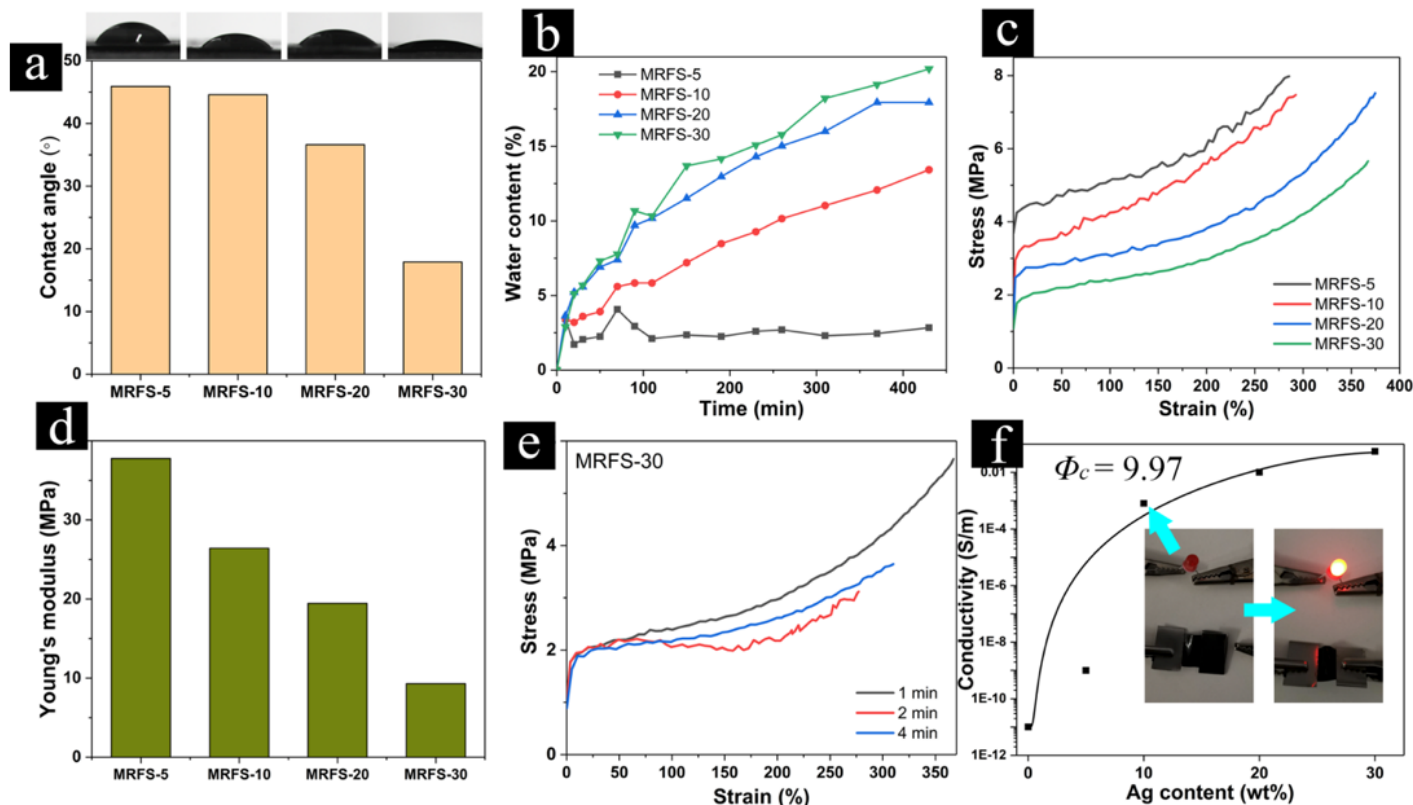


Figure 2

(a) Contact angle measurements and photographs of deionized water on the surface of MRFS. (b) Evolution of water adsorption as a function of time for MRFS at 75% RH. (c) Typical stress-strain curves of MRFS tested at ambient RH (~ 70%). (d) Young's modulus of MRFS determined from stress-strain curves. (e) Typical stress-strain curves of MRFS-30 with the weaker mechanical properties with different place time in the air. (f) Conductivity as a function of Ag content for HSHRF at an ambient RH (~ 70%) when the resistance did not change. Insets showed the luminescence of LED lamp: LED lamp was not lighting in open circuit; LED lamp was lighting in HSHRF-10 into the circuit.

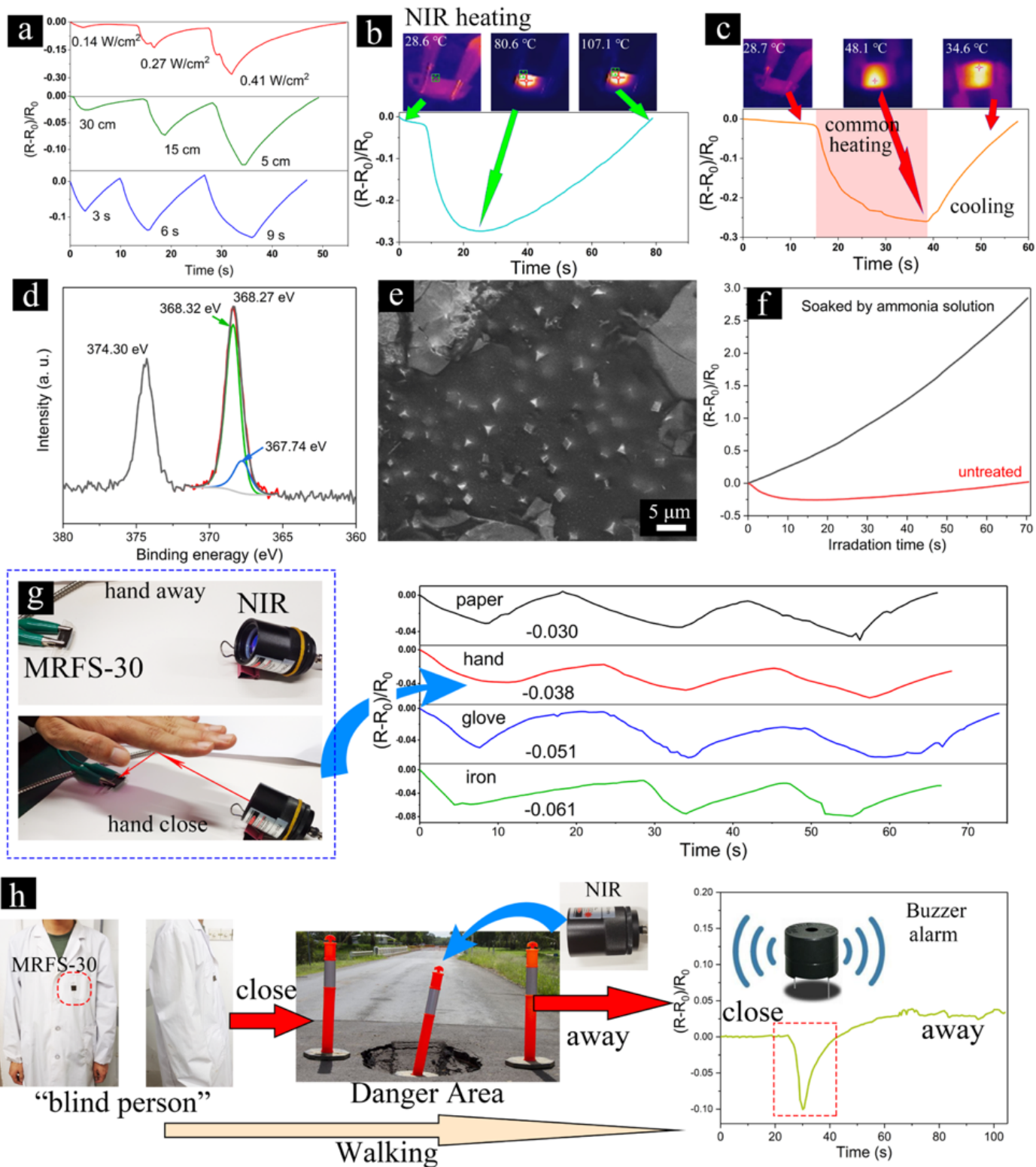


Figure 3

(a) The resistance changes under NIR irradiation in variable parameter (power, distance and time), where R_0 is the initial resistance at $t=0$; R is value of resistance change with time. (b) The resistance changes under NIR irradiation with time. (c) The resistance changes by common heating method and then cooling. (d) XPS spectrum of MRFS-30. (e) SEM images of the top surface of MRFS-30. (f) The resistance

changes under NIR irradiation for MRFS-30 soaked by ammonia solution and untreated MRFS-30. (g) and (h) fabricated infrared proximity sensor for different applications.

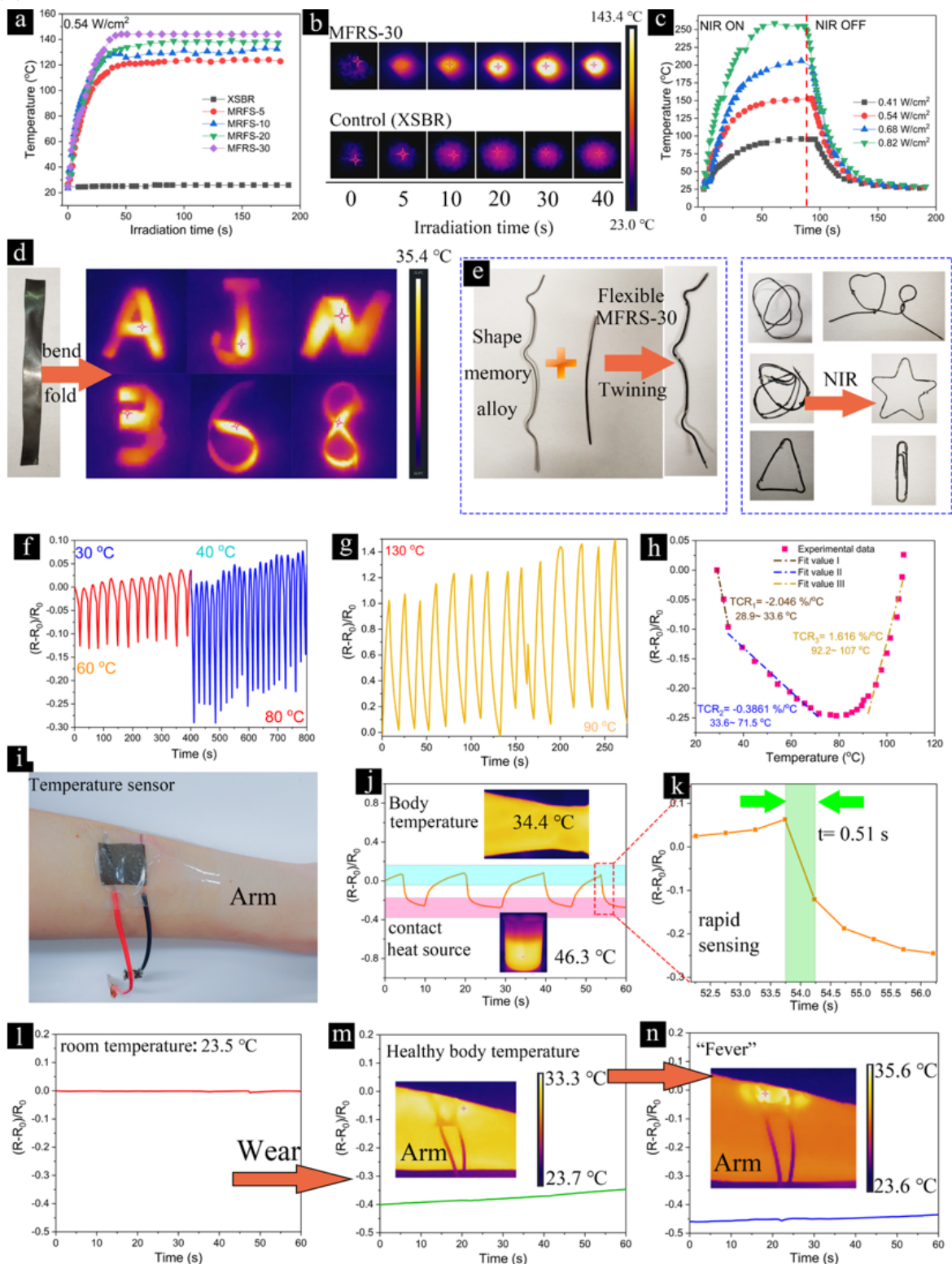


Figure 4

(a) Photothermal conversion of MRFS with different nanosilver content under 808 nm NIR (0.54 W/cm²), irradiation distance at 10 cm. (b) Photothermal images of MRFS-30 and XSBR under 808 nm laser irradiation (0.54 W/cm²), irradiation distance at 10 cm. (c) Photothermal conversion of MRFS-30 under

different NIR power (0.41, 0.54, 0.68 and 0.82 W/cm²), irradiation distance at 10 cm. (d) The flexible rubber film can be bended and folded into diverse shapes as well as a photothermal conversion under a 0.2 W/cm² NIR irradiation. (e) The flexible rubber film can be twinned on the surface of SMA to endow it with photothermal conversion under a 0.82 W/cm² NIR irradiation. (f) The resistance changes of MRFS-30 between 30 and 60, 40 and 80 °C under a 0.41 W/cm² NIR irradiation, irradiation distance at 10 cm. (g) The resistance changes of MRFS-30 between 90 and 130 °C under a 0.41 W/cm² NIR irradiation, irradiation distance at 10 cm. (h) Relative resistance changes of MRFS-30 upon increasing temperature from room temperature to 107 °C under a 0.41 W/cm² NIR irradiation, irradiation distance at 10 cm. (i) A wearable temperature sensor was fabricated by MRFS-30. (j)~ (k) Monitoring the temperature changes by contact with heat source (46.3 °C hot water). (l)~ (n) wearable temperature sensor was used to monitor the body temperature changes for room temperature (l), healthy body temperature (m) and “fever” temperature (n).

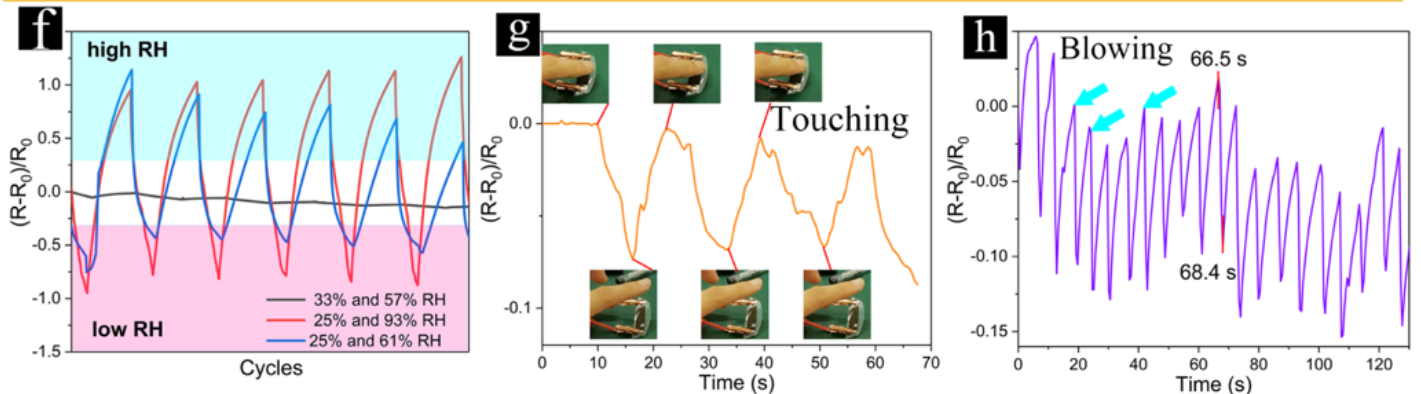
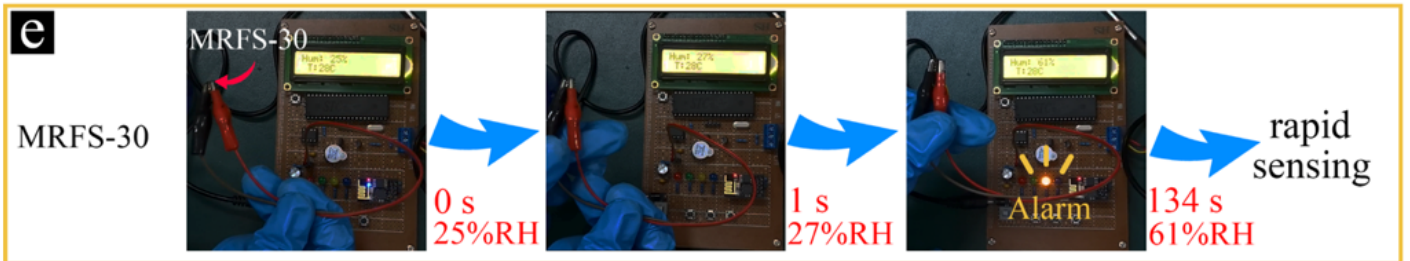
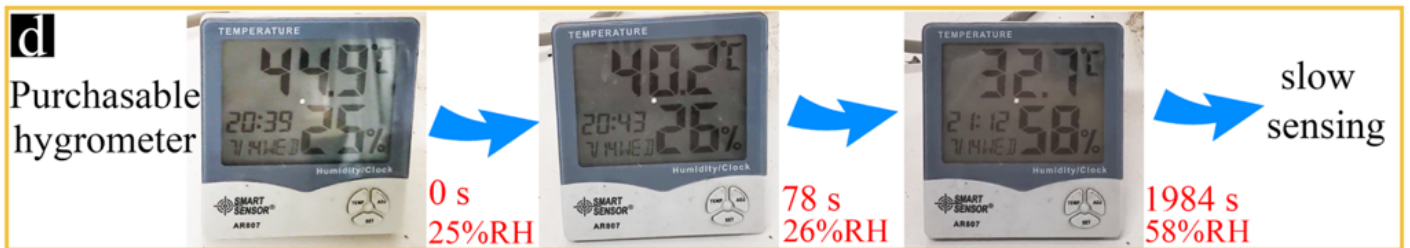
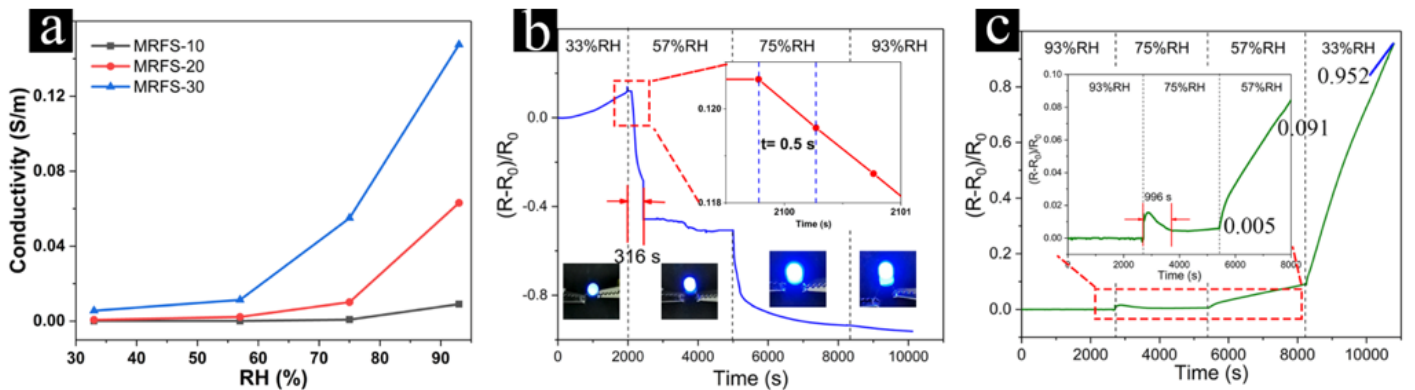


Figure 5

(a) The conductivity of MRFS at different RH for 900 s. (b) The change of $(R-R_0)/R_0$ of MRFS-30 with time from low RH to high RH. (c) The change of $(R-R_0)/R_0$ of MRFS-30 with time from high RH to low RH. (d) A hygrometer was taken from a 50 °C oven with 25% RH, then it was placed in ambient humidity (58% RH). The RH on the screen gradually changed with time. (e) HSHRF-30 was taken from dry surrounding with 25% RH, then it was placed in ambient humidity (61% RH). The RH on the screen gradually changed with time. (f) The cyclic humidity changes between 57% RH for 120 s and 33% RH for 120 s, between 25% RH for 120 s and 61% RH for 60 s for HSHRF-30, between 25% RH for 120 s and 93% RH for 60 s. (g) Sensitive response to small amount of moisture on our fingers. (h) Sensitive response to moisture from our blowing.

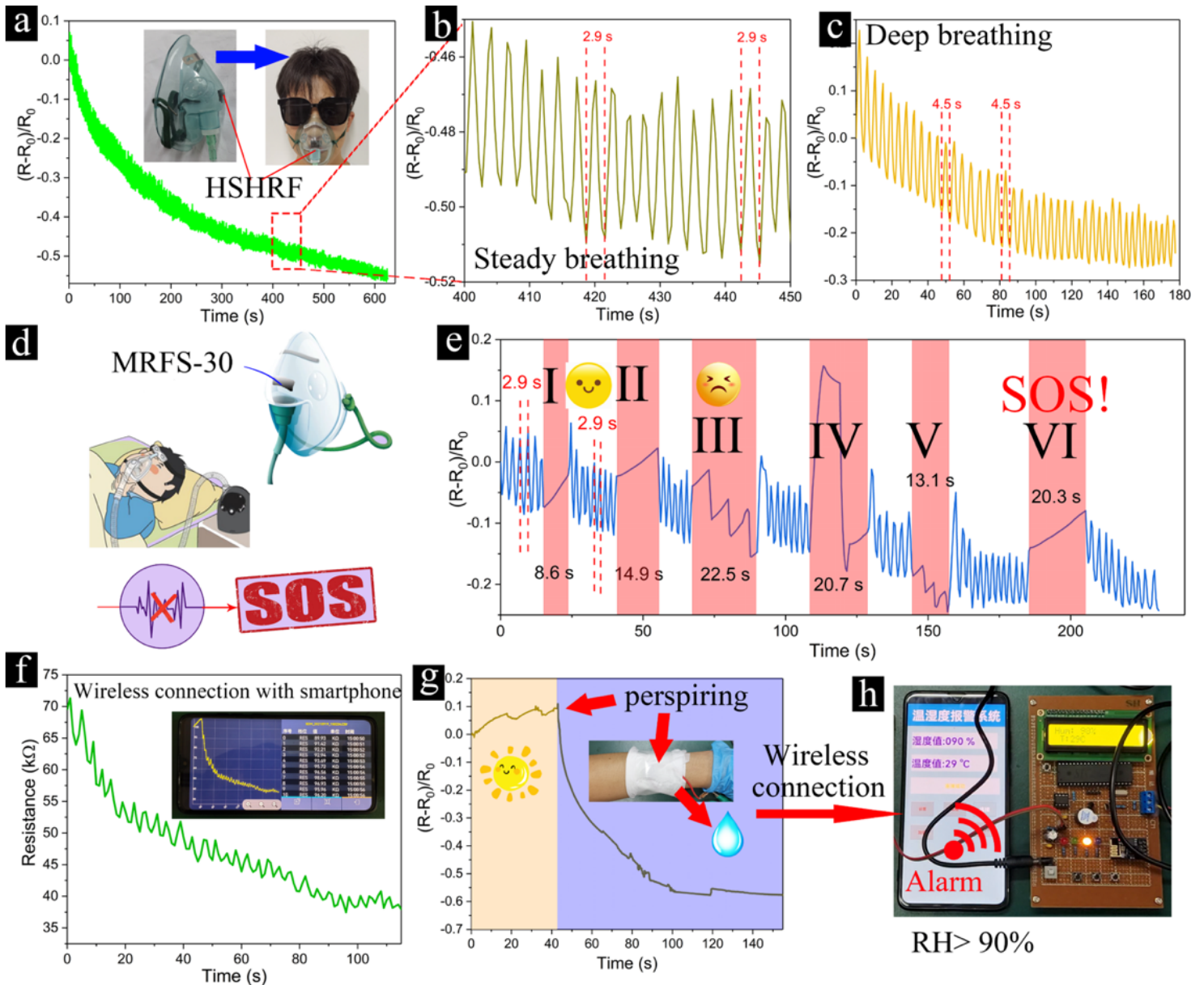


Figure 6

(a) and (b) Detection of normal breathing with an identical interval. Insert is the design of a respiratory detection device for an emergency. (c) Detection of deep breathing. (d) A respiratory detection for an emergency. (e) Real-time monitoring of healthy and dangerous breathing. (f) The respiratory monitoring can be conducted by the wireless connection with smartphone. (g) and (h) The MRFS-30 can be used to monitor the bodily perspiration by the wireless connection with smartphone.

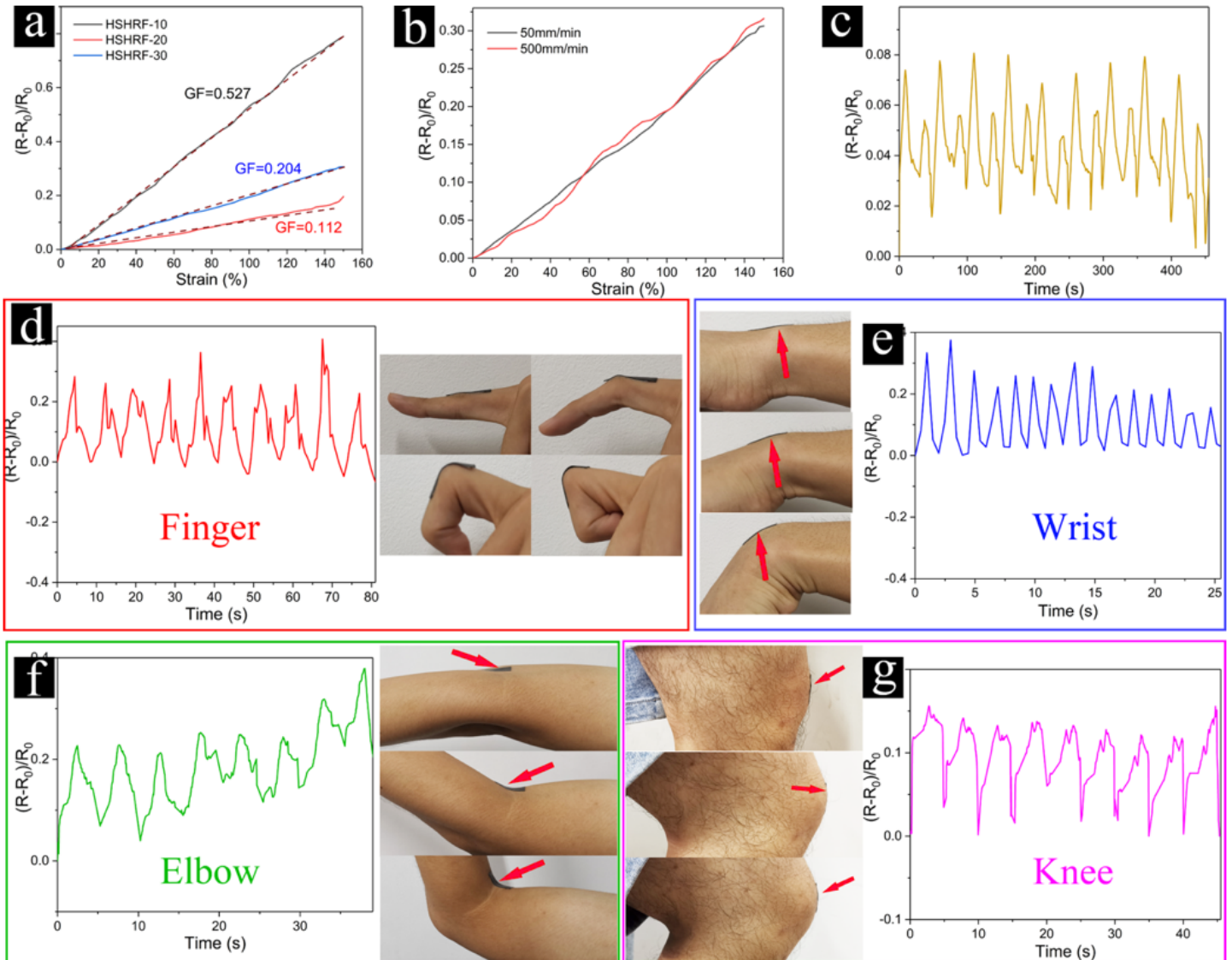


Figure 7

The function of strain response for MRFS. (a) Typical relative resistance versus strain curve of MRFS at a stretching rate of 50 mm/min. (b) Typical relative resistance versus strain curve of MRFS-30 at stretching rates of 50 and 500 mm/min. (c) Relative resistance variation under the cyclic strain of 0-25%. (d), (e), (f) and (g) Monitoring joint movement including finger, wrist, elbow and knee, respectively.

Supplementary Files

This is a list of supplementary files associated with this preprint. Click to download.

- [SupportingInformation.docx](#)
- [MovieS1.mp4](#)
- [MovieS2.mp4](#)
- [MovieS3.mp4](#)
- [MovieS4.mp4](#)
- [MovieS5.mp4](#)